Calibration of Fixed-Wing UAV Aerodynamic Coefficients with Photogrammetry for VDM-based Navigation

Gabriel Laupré, Jan Skaloud, *Geodetic Engineering Laboratory, Swiss Federal Institute of Technology Lausanne (EPFL)*

BIOGRAPHY

Gabriel Laupré joined the geodetic engineering laboratory at the Swiss Federal Institute of Technology Lausanne in 2017. His research focuses on methods for the autonomous navigation of UAVs. He graduated from the same university in 2015 with a Master in communication systems and a Minor in space technologies.

Jan Skaloud is a senior scientist and lecturer at the Swiss Federal Institute of Technology Lausanne in the field of integrated technologies for navigation, mobile mapping and remote sensing. He leads international working groups in geodesy (IAG) and photogrammetry and remote sensing (ISPRS).

ABSTRACT

Autonomous navigation is a crucial aspect for fixed-wing unmanned aerial vehicle operation when encountering disturbance or denial of GNSS signal reception. Vehicle dynamic model - based navigation improves the performance of methods based exclusively on introspective sensors (e.g., inertial, pressure) by incorporating mathematical models of aerodynamic forces and moments into the final navigation solution. Such an approach, however, requires model-coefficients that are calibrated to the specific vehicle being operated. We propose augmenting the self-calibration of these coefficients with additional observations derived from an on-board camera via photogrammetry. We confirm experimentally that irregular yet precise observations of vehicle absolute attitude obtained through such techniques greatly improve the determination of some aerodynamic coefficients that in turn reduce the error in autonomous positioning under GNSS signal outage.

I. INTRODUCTION

The increasing number of unmanned aerial vehicles (UAVs) being operated in public airspace has triggered the adoption of new regulations to effectively manage this activity. These regulations consider many factors, among them safety features such as return-to-home options, which ensure the secure landing of UAVs under compromised circumstances e.g. low-battery, loss of communication or degradation of weather or navigation performance. Considering the latter, in an absence of exteroceptive sensors (such as as cameras, lidars) or their reduced perception due to fog, darkness, absorption, such security procedures are compromised when a UAV loses satellite signal reception due to RF interference, spoofing or jamming, or simply physical obstructions. Hence, improving the quality of autonomous (interoceptive) navigation remains a dominant research topic, especially for methods that achieve this without the use of additional sensors.

A relatively new approach to autonomous navigation utilising a vehicle dynamic model (VDM) in a special architecture has demonstrated potential to significantly improve positioning accuracy of small fixed-wing UAV within GNSS denied or perturbed environments as compared to inertial-based navigation [1]. In mapping flights with precise Real-Time Kinematic or Post-Processed Kinematic (RTK/PPK) GNSS positioning, this approach also improves the estimation of direct orientation (attitude) [2]. However, VDM-based navigation utilizes aerodynamic-model coefficients which are specific to the aircraft geometry that is being controlled. Thus the precise estimation of such coefficients is required for each geometry that VDM is applied to. An in-flight calibration procedures estimating these coefficients under nominal GNSS conditions represents an attractive (and inexpensive) alternative to achieve such a goal. Prior investigations of this approach address certain challenges in separating the estimates of aerodynamic coefficients relating to certain forces or moments [3]. The estimation of moments in particular proved to be especially difficult and required multiple iterations [4]. This motivates the use of external and precise observations of absolute attitude during a calibration flight. Photogrammetry represents one of the best options available to obtaining such information at 0.01 deg-level or better at an extra weight of $\tilde{0}.1\ kg$ (camera) [5].

The continuation of the paper is organized as follows: A brief review of commonly used reference frames is provided. Then, Sec. II. describes the steps to obtain accurate attitude references via photogrammetry, Sec. III. summarizes the general concepts of vehicle dynamic based-navigation and Sec. IV. details the experimental setup. Finally, Sec. V. exposes the practical results when using attitude references as observations and Sec. VI. summarizes the findings.

Frames Definition

Tab. 1 summarizes the coordinate frames and their respective usage in VDM and photogrammetry (PHOT) related implementations.

Table 1: Frames used in photogrammetry (PHOT) and VDM-based navigation. The possible usage of INS/GNSS integrated trajectory in photogrammetry involves frames marked as (x).

Coordinate frame	subscript	PHOT	VDM
inertial	i		x
Earth-Center Earth-Fixed	e	(x)	x
local-level	l	(x)	x
camera	c	x	
IMU	b_u	(x)	x
local-mapping	l_0	x	
body (vehicle)	b		x
wind	w		x

The *inertial frame* is a non-accelerated reference system, either at rest or subject to uniform translational motion. Newton's first and second laws of motion are relevant in such frame.

The *Earth-fixed-Earth-centered frame (ECEF)* is a terrestrial equatorial system defined with its origin as the geocenter, the first axis x_1^e pointing towards the Greenwich meridian, the third x_3^e towards the mean rotation axis of the earth and the second x_2^e completing a right-handed Cartesian system. We consider the realisation of this frame corresponding to WGS-84.

The origin of a *local-level frame* is set on the surface of an ellipsoid (e.g. corresponding to WGS-84). In so called local NED, the first axis x_1^l points to the geographic North, the second axis x_2^l to the East and the third axis x_3^l points down in the direction of surface normal. In the East-North-Up (ENU) setup, the first two axis are swapped while the direction of the 3$^{\text{rd}}$ is reversed.

The *body frame* is often used to express the relative attitude of a object with respect to a local level frame. Its origin is located within an object at a specific point. In aerial navigation, its location is commonly where an inertial navigation system is installed. However in this work, a body frame will be defined at the center of gravity of the platform for the VDM realisation. The axes form a right-handed Cartesian frame with the first x_b pointing forwards, the second axis y_b towards the right wing and the third z_b downwards.

The *camera frame* is defined with the image sensor principal axes. When calibrating the camera's exterior and interior orientation parameters, the bore-sight and also possibly the lever-arm between the camera and an IMU can be determined. Accounting for these parameters allows for camera poses to be transformed to body-frame poses.

The *imu frame* coincides with the triplet of accelerometer and gyroscope axes in the IMU. Like the camera frame, by compensating for the bore-sight and lever arm with respect to the body frame, the expression of an observation in a local level frame with respect to the IMU frame will be equal to its expression in the b frame.

The *local-mapping frame* is a Cartesian frame, tangential to the ellipsoid at an arbitrary origin close to the mapping area. The image poses are expressed with respect to this frame, usually in ENU orientation.

The *wind frame* has its first axis in the direction of the airspeed $\mathbf{V}$, and its orientation with respect to the body frame is defined by two angles: the angle of attack α and the side-slip angle β. The airflow velocity due to the UAV's inertial velocity $\mathbf{v}$ and wind velocity $\mathbf{w}$ is denoted by the airspeed vector. $\mathbf{V} = \mathbf{v} - \mathbf{w}$. Its definition is presented in Fig. 1 together with the body and local-mapping frames (the latter in NED orientation). The camera and IMU frame are also depicted on the right side.

II. ATTITUDE REFERENCES FROM PHOTOGRAMMETRY

1. Procedure

Four main steps are necessary to produce precise attitude observations from overlapping images acquired by the UAV which can later be used to improve the calibration of the UAV aerodynamic coefficients:

1. First, the position and attitude (pose) of each image are approximately obtained from the camera exposure-times using onboard sensors and INS/GNSS integrated trajectory with cm-level (RTK/PPK) relative GNSS positioning and sufficient flight geometry (overlap, altitude variation).
2. Second, the photogrammetry-suite software analyses each image separately to detect key-points, the centroids of local image features. Then, with the help of approximated values of pose and camera interior-orientation, the software

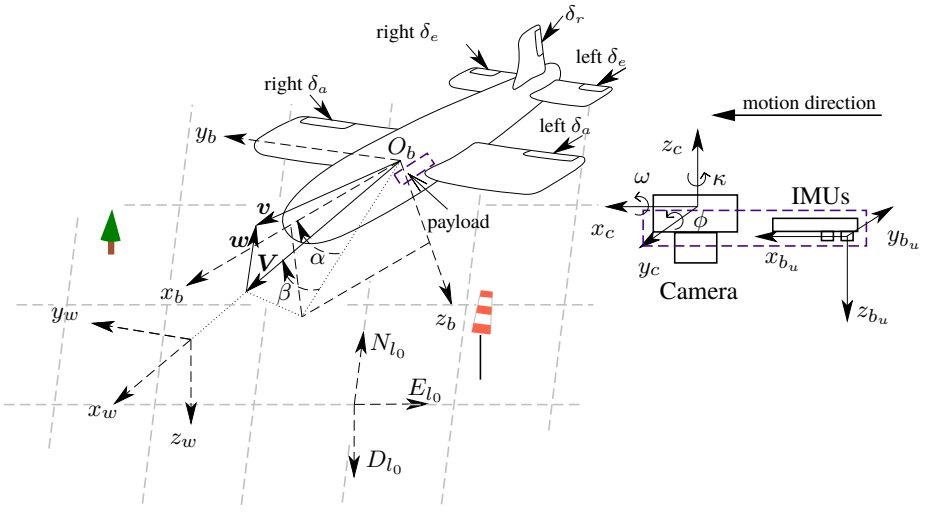

Figure 1: Local level, body, and wind frames with airspeed $\mathbf{V}$, wind velocity $\mathbf{w}$, and UAV velocity $\mathbf{v}$ [3]

determines correspondences (matches) between some of these points on several images.

3. Third, the image-observations of matched key-points are confronted with approximate observations of camera poses in a bundle-adjustment (BA). At this point, the observations of signalized points, so called ground control points (GCPs), can be added (both in object and image space). This additional information improves the concurrent determination of camera poses and camera interior orientation but is not necessarily indispensable if the geometry of the image configuration is strong and the aerial control during flight (via GNSS or INS/GNSS) is of sufficient accuracy [5].
4. The final step transforms the adjusted camera exterior orientation at these instances to the IMU or body frame to use the absolute attitude references in the estimator. The last step is detailed with its implementation in Sec. 2. on a particular flight.

2. Transformation back to IMU-navigation (l) frame

The UAV working area covers a small portion of the Earth surface. Thus, a local tangent frame (l_0) with ENU axes orientation can be used (with negligible influences of Earth curvature) as the mapping frame. Its origin, denoted as ENU_o is set either at the center of the mapping zone or at its extremity to keep positive coordinates. After running the photogrammetry process and its bundle adjustment with INS/GNSS input, the camera attitude $R_{l_o}^{c(j)}$ can be obtained for each photo $j \in [j = 1..J]$.

Eventually, to obtain IMU attitudes $R_{b_u(i)}^{NED_i}$ from oriented photos $R_{l_0}^{c(j=i)}$, a sequence of transformations must be performed:

$$R_{b_u}^{l_i} = R_e^{l_i}\left(\varphi_i, \lambda_i\right) \cdot R_{l_0}^{e}\left(\varphi_0, \lambda_0\right) \cdot T_{ENU}^{NED} \cdot \left(R_c^{b_u} \cdot R_{l_0}^{c(i)}\right)^T \tag{1}$$

The camera attitude is rotated from the mapping frame (here local-Cartesian system, ENU) back to navigation-frame (local-level on a reference ellipsoid, NED). This process is somewhat subtle when the mapping-frame includes projection and/or national reference-frame [6].

The bore-sight between the camera and the IMU representing their orientation offset (R_c^b in Eq.1) was estimated within the bundle adjustment, possibly in a different flight using INS/GNSS derived orientation parameters [7].

Further, the matrix T_{ENU}^{NED} in Eq. 1 defined as

$$T_{ENU}^{NED} = \begin{bmatrix} 0 & 1 & 0 \\ 1 & 0 & 0 \\ 0 & 0 & -1 \end{bmatrix}^T \tag{2}$$

transforms the axis orientation between NED and ENU.

The matrix

$$R_{l_o}^{e} = \begin{bmatrix} -sin(\varphi_0) \cdot cos(\lambda_0) & -sin(\lambda_0) & -cos(\varphi_0) \cdot cos(\lambda_0) \\ -sin(\varphi_0) \cdot sin(\lambda_0) & cos(\lambda_0) & -cos(\varphi_0) \cdot sin(\lambda_0) \\ cos(\varphi_0) & 0 & -sin(\varphi_0) \end{bmatrix} \tag{3}$$

is a constant rotation from mapping-local frame to e frame and

$$R_{e}^{NED_i} = R_{NED}^{e}\left(\varphi_i, \lambda_i\right)^T \tag{4}$$

where (φ_i, λ_i) represent the IMU position at the time at which the image was taken.

The procedure to obtain attitude reference updates from IMU and camera data, camera EO and IMU errors calibration and, precise INS/GNSS integration with photogrammetry treatments, is schematically depicted in Fig. 2. The superscript ˜ and ˆ are used to specify estimated and updated results, respectively.

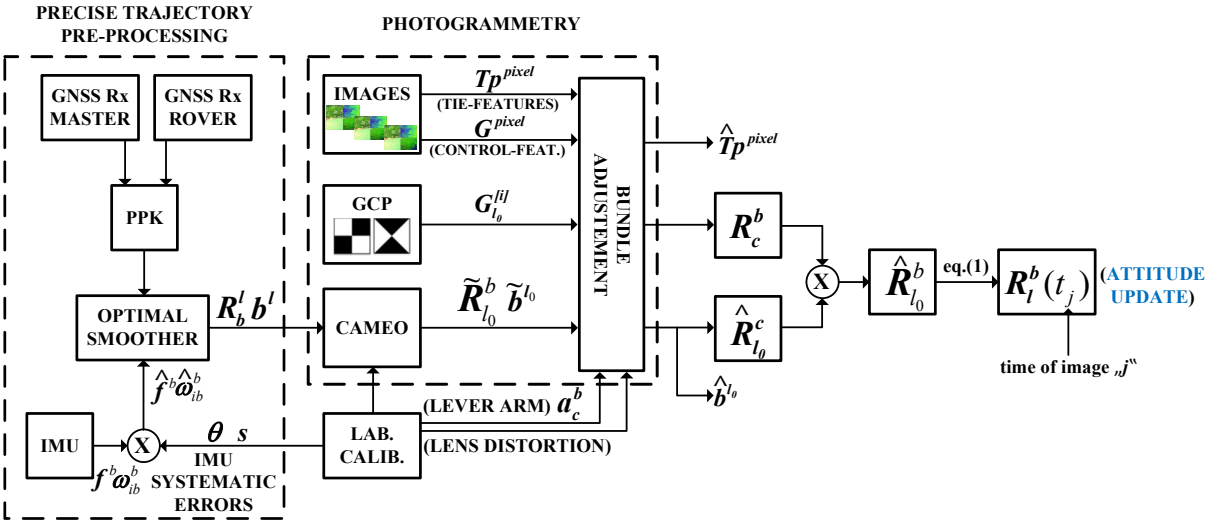

Figure 2: Steps required to obtain attitude updates in the body-frame using the precise pre-processing trajectory treatment and photogrammetry

III. VEHICLE DYNAMIC MODEL

This section presents the implemented VDM-based navigation and its Extended Kalman Filter (EKF) [8] used as an estimator. This filter is adapted to include attitude observations as additional measurements. While the presented material is limited to general comprehension of the VDM-based navigation architecture, the details on its derivation are contained in [3, 9].

1. Rigid body motion with VDM

The rigid body is modeled in an arbitrary 3D space affected by the Earth's gravity via the specific forces $\mathbf{f}$, and moments $\mathbf{M}$. These are described via a set of first-order differential equations (6) – (9) considering the Earth's physics (i.e., the rotation, curvature and normal gravity), the resolution of which provides the following *navigation states*

$$\mathbf{X}_n = \left[\mathbf{r}_e^{l\,T}, \mathbf{v}_e^{l\,T}, \mathbf{q}_b^{l\,T}, \boldsymbol{\omega}_{ib}^{b\,T}\right]^T \tag{5}$$

where the vector $\mathbf{r}_e^l = [\phi, \lambda, h]^T$ represents the platform position (origin of body frame) in ellipsoidal coordinates, $\mathbf{v}_e^l = [v_N, v_E, v_D]^T$ is the velocity local-level (NED) frame, $\mathbf{q}_b^l = [q_0, q_1, q_2, q_3]^T$ is the quaternion representation of attitude (body frame with respect to the local frame), and $\boldsymbol{\omega}_{ib}^b = [\omega_x, \omega_y, \omega_z]^T$ is the angular velocity vector between body and inertial frame, expressed in

the body frame. The evolution of *navigation states* in time and space are described by

$$\dot{\mathbf{r}}_e^l = D^{-1}\mathbf{v}_e^l \tag{6}$$

$$\dot{\mathbf{v}}_e^l = C_b^l\mathbf{f}^b + \mathbf{g}^l - (\Omega_{el}^l + 2\Omega_{ie}^l)\mathbf{v}_e^l \tag{7}$$

$$\dot{\mathbf{q}}_b^l = \frac{1}{2}\mathbf{q}_b^l \otimes \left[\boldsymbol{\omega}_{lb}^b\right]_q \tag{8}$$

$$\dot{\boldsymbol{\omega}}_{ib}^b = \left(I^b\right)^{-1}\left[\mathbf{M}^b - \Omega_{ib}^b(I^b\boldsymbol{\omega}_{ib}^b)\right], \tag{9}$$

where any $\mathbf{\Omega}_{pq}^r$ is a skew-symmetric matrix representation of the associated angular-rate vector of the q-frame with respect to the p-frame expressed in the r-frame. The $\otimes$ operator defines quaternion cross-products as in [10]. In Eq. (6), the matrix D^{-1} is a function of the ellipsoid curvatures, height and longitude. In Eq. (7), the rotation matrix C_b^l can be expressed as a known function of the quaternion $\mathbf{q}_b^l$ [11]. In Eq. (8), the skew-matrix $\boldsymbol{\omega}_{lb}^b$ is calculated as

$$\boldsymbol{\omega}_{lb}^b = \boldsymbol{\omega}_{ib}^b - \left(C_b^l\right)^T\left(\boldsymbol{\omega}_{ie}^l + \boldsymbol{\omega}_{el}^l\right), \tag{10}$$

The rigid body motion can be obtained for a general platform by resolving the differential equations with the knowledge of initial conditions and forcing inputs of specific forces $\mathbf{f}$, external moments $\mathbf{M}$, and the Earth gravity $\mathbf{g}$. For a fixed-wing UAV, an aerodynamic model (after [12]) defines the specific force vector $\mathbf{f}$ and the moment vector $\mathbf{M}$ as

$$\mathbf{f}^b = \frac{1}{m}\left(\begin{bmatrix}F_T\\0\\0\end{bmatrix} + C_w^b\begin{bmatrix}F_x^w\\F_y^w\\F_z^w\end{bmatrix}\right), \qquad \mathbf{M}^b = \begin{bmatrix}M_x^b\\M_y^b\\M_z^b\end{bmatrix} \tag{11}$$

with m denoting the mass of the UAV. Thrust, drag, lateral, and lift forces (F_T, F_x^w, F_y^w, and F_z^w, respectively) are the components of aerodynamic forces and, roll, pitch, and yaw moments (M_x^b, M_y^b, and M_z^b, respectively) are the aerodynamic moments. While the thrust force (along x_b-axis) and all moment components are expressed in body frame, lift, lateral, and drag forces are expressed in the wind frame:

$$F_T^b = \rho n^2 D^4\left(C_{F_T1} + C_{F_T2}J + C_{F_T3}J^2\right) \tag{12}$$

$$F_x^w = \bar{q}S\left(C_{F_x1} + C_{F_x\alpha}\alpha + C_{F_x\alpha2}\alpha^2 + C_{F_x\beta2}\beta^2\right) \tag{13}$$

$$F_y^w = \bar{q}S\left(C_{F_y1}\beta\right) \tag{14}$$

$$F_z^w = \bar{q}S\left(C_{F_z1} + C_{F_z\alpha}\alpha\right) \tag{15}$$

$$M_x^b = \bar{q}Sb\left(C_{M_xa}\delta_a + C_{M_x\beta}\beta + C_{M_x\tilde{\omega}_x}\tilde{\omega}_x + C_{M_x\tilde{\omega}_z}\tilde{\omega}_z\right) \tag{16}$$

$$M_y^b = \bar{q}S\bar{c}\left(C_{M_y1} + C_{M_ye}\delta_e + C_{M_y\tilde{\omega}_y}\tilde{\omega}_y + C_{M_y\alpha}\alpha\right) \tag{17}$$

$$M_z^b = \bar{q}Sb\left(C_{M_z\delta_r}\delta_r + C_{M_z\tilde{\omega}_z}\tilde{\omega}_z + C_{M_z\beta}\beta\right) \tag{18}$$

where the UAV geometric proprieties b, S, $\bar{c}$, and D are the wing span, wing surface, mean aerodynamic chord, and propeller diameter, respectively. The air density is denoted by ρ, while $\bar{q}$ is the dynamic pressure defined as $\rho V^2/2$, and J is defined as $V/(D\pi n)$ with n denoting the propeller rotation speed. The angular velocities are defined as $\tilde{\omega}_x = b\omega_x/(2V)$, $\tilde{\omega}_y = \bar{c}\omega_y/(2V)$, and $\tilde{\omega}_z = b\omega_z/(2V)$. The axes dependant forces and moment-related aerodynamic coefficients are represented by $C_{\ldots}$'s. The deflections of aileron, elevator, and rudder are denoted respectively by δ_a, δ_e, and δ_r.

2. Navigation system

VDM serves as the main process model within the filter as shown in Fig. 3. An EKF is chosen to estimate corrections to the states ($\Delta\mathbf{X}$) and the associated covariance matrix (P). More detailed descriptions of process models, observation models, and their linearization for the proposed VDM-based navigation can be found in [3].

As depicted in Fig. 3, the VDM provides the navigation solution ($\mathbf{X}_n$), which is updated as part of the augmented state vector $\mathbf{X}$ (introduced in Equation (19)) based on available observations.

IMU data are treated as observations while other sensor data such as airspeed, optic flow, and magnetometer data, or precise attitude references for this particular study, can also be integrated within the navigation system.

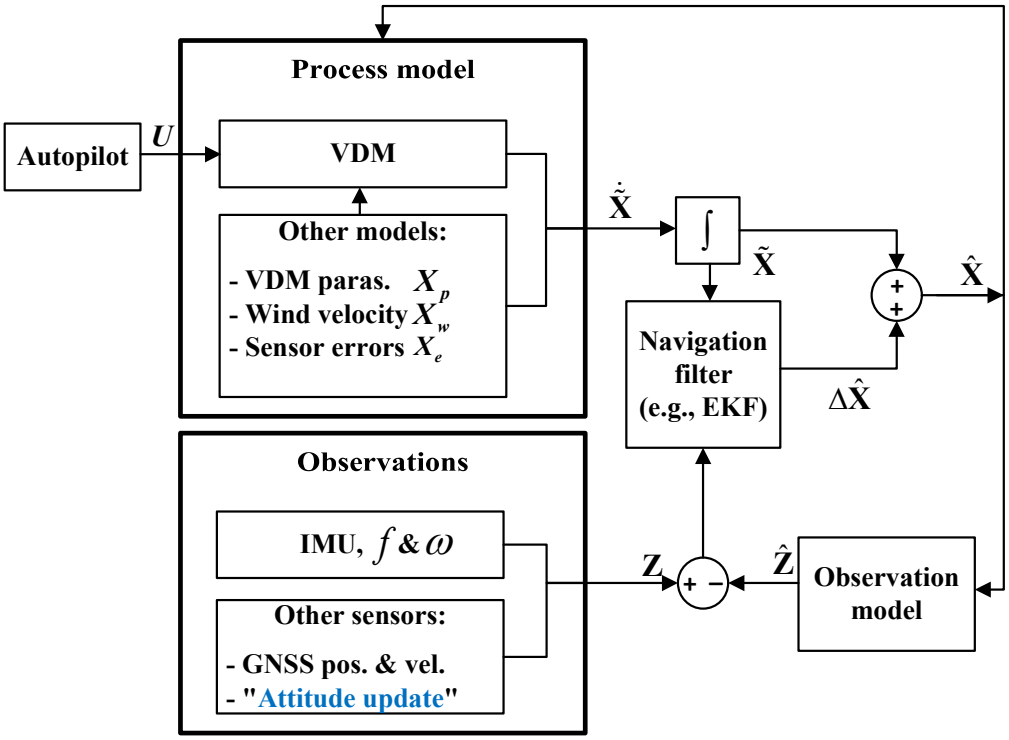

Figure 3: VDM-based navigation filter architecture ($\tilde{\mathbf{X}}_k \equiv \hat{\mathbf{X}}_{k|k-1}$), adapted from [3]

The VDM is fed with the UAV control input ($\mathbf{U}$) as commanded by the autopilot and is therefore always available. Wind velocity ($\mathbf{X}_w$) is also required, which can be estimated within the navigation system, even in the absence of airspeed sensors, which is the case here [13]. The required VDM parameters ($\mathbf{X}_p$) can be pre-calibrated and used as fixed values in the navigation system or estimated/refined in-flight.

IMU errors ($\mathbf{X}_e$) generalized as biases are included within the augmented states vector to be estimated. The augmented state vector $\mathbf{X}$ includes therefore the navigation states $\mathbf{X}_n$, the VDM parameters $\mathbf{X}_p$, the wind velocity components $\mathbf{X}_w$ and the sensor error states $\mathbf{X}_e$.

$$\mathbf{X} = [\mathbf{X}_n^T, \mathbf{X}_p^T, \mathbf{X}_w^T, \mathbf{X}_e^T]^T \tag{19}$$

The mass (m) and moments of inertia $\mathbf{I}^b$ are excluded from $\mathbf{X}_p$ since they appear as scaling factors in the model, meaning they are completely correlated with the already included aerodynamic coefficients [3]. The platform-dependant geometric measures are also excluded, because they can be determined a priori with much lower uncertainty compared to aerodynamic coefficients.

IV. EXPERIMENTAL SETUP

The fixed-wing platform experimental setup is depicted in Fig. 4. The same setup is used for both the calibration of the UAV aerodynamic coefficients and their performance evaluation in autonomous navigation. This section discusses the experimental setup characteristics.

1. Platform

As displayed on Fig. 4, the payload carried by small fixed-wing aircraft (TOW < 3 kg, [5]) is composed of: i) a custom, 20 Mpx camera for aerial photogrammetry developed by IGN, France [14] with Zeiss Biogon 35 mm lens, ii) a Gecko4Nav redundant IMU board [15] with two Intersense NavChip MEMs IMUs, iii) a Topcon B110 GPS/GLONASS L1/L2 receiver.

All data from Gecko4Nav are stored in internal memory together with select GNSS data. The on-board GNSS multi-frequency (GPS/GLONASS) receiver Topcon B110 has its own storage for all observations including phase, phase rate and pseudo-ranges on multiple frequencies. These are required for obtaining cm-level positioning and cm/s velocity accuracy that are used for

Figure 4: Fixed-wing platform with 5 control surfaces (left), PixHawk AP, precise GNSS and a payload containing DigiCAM (top-right), Gecko board (bottom-right) with two Navchip IMUs and 32-bit micro computer.

calibration as well as for reference purposes. This receiver time-tags the pulse signalized events of camera shutter openings. It provides also the precise pulse per second (PPS) to Gecko4Nav board and the autopilot (PixHawk) for associating IMU data and autopilot (Pixhawk) control commands in GPS time scale, respectively.

2. Calibration

A flight of about 33 min. duration, henceforth referred to as "IGN8", was conducted to utilize the photogrammetry solution to improve the estimation of the platform-dependant aerodynamic coefficients. The flight characteristics are summarized in Tab. 2. In total, 440 images during 26 flight-lines at 2 flight levels (120 m and 150 m AGL) in a block mission geometry were considered. The longitudinal overlap was approximately 65% while the lateral overlap was approximately 45%. The bundle adjustment was performed with the Metashape software (previously PhotoScan) from AgiSoft [1], using additional inputs from precise aero-control from INS/GNSS integrated trajectory and about 20 GCPs. The image coordinates of signalized GCPs were obtained automatically by mask-fitting with an accuracy of about 0.1 pixel.

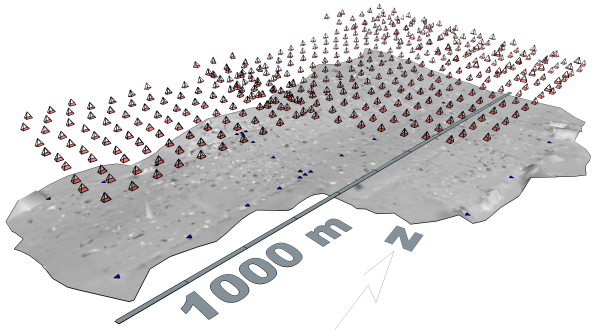

Figure 5: Bundle adjustment. Image from [16]

Table 2: Calibration flight details.

Flight name	IGN8
Geometry	Block
Images	440
Flight lines	26
Flight levels	2
Long. overlap [%]	65
Lat. overlap [%]	45
External control	GCP
No.	21
1 σ (xy,z) [mm]	10, 15

Fig. 5 shows the camera orientations in red triangles at the instant an image was taken and the GCPs in blue triangles on the ground. The mean camera orientation uncertainties over all images after the bundle adjustment are (3, 3, 1.4) $arcsec$ (i.e., $\approx$0.002 deg) for the angle around the x_c (ω) , y_c (ϕ), and z_c (κ) axis respectively. Overall, more than 400 oriented images were used to obtain absolute attitude measurements in Sec. V. The INS/GNSS integrated trajectory is used for approximating camera poses in each picture prior bundle adjustment. These were also used for initialising the VDM-based estimator within the calibration flight.

[1]AgiSoft PhotoScan Professional (Version 1.2.6) (Software). (2016*)Retrieved from http://www.agisoft.com/downloads/installer/

V. RESULTS AND DISCUSSION

1. Parameter calibration

The approximate (initial) values of the aerodynamic coefficients are refined via EKF within a large portion of the IGN8 flight ($\backsim$31 minutes), henceforth referred to as the calibration phase, using as observations the raw IMU data (always) and a) GNSS (position/velocity) only; b) GNSS plus photogrammetry.

The impact of photogrammetry can first be observed through the difference in the estimation of states. The change in some of the states of interest namely, VDM parameters $\mathbf{X}_p$, IMU errors $\mathbf{X}_e$ and wind $\mathbf{X}_w$, after convergence, i.e. at the end of the VDM-calibration phase, are compared in the following subsections.

Aerodynamic coefficients

The initial values for aerodynamic model coefficients are taken from [12], while adapting the physical parameters to match those of the experimental UAV (Fig. 4). Their initial uncertainty is set to 2% of their values. The parameters are listed in the 1^{st} and 5^{th} column of Tab. 3 for forces C_F and moments C_M, respectively.

Table 3: Initial and estimated VDM parameters at the end of the calibration phase.

Forces	Init. Value	GNSS only	GNSS+CAM	Moments	Init. Value	GNSS only	GNSS+CAM
C_{FT_1}	0.00262	0.00301	0.00349	C_{Mx_a}	-0.00236	-0.012	-0.012
C_{FT_2}	-0.05	-0.0326	-0.0601	C_{Mx_β}	0.00254	0.0058	0.0061
C_{FT_3}	2.23	4.37	4.27	$C_{Mx_{\omega_x}}$	-0.0465	-0.161	-0.1536
C_{Fz_1}	-0.125	-0.049	-0.091	$C_{Mx_{\omega_z}}$	-0.0219	0.0195	0.0161
C_{Fz_α}	-4.76	-18.7	-18.7	C_{My_1}	0.0215	-0.026	-0.026
C_{Fx_1}	-0.205	-0.485	-0.386	C_{My_e}	0.27	0.370	0.369
C_{Fx_α}	-0.728	0.507	1.451	C_{My_α}	-0.657	-1.150	-1.121
$C_{Fx_{\alpha_2}}$	-0.0538	-0.0551	-0.0537	$C_{My_{\omega_y}}$	-9.16	-17.93	-18.96
$C_{Fx_{\beta_2}}$	0.568	1.06	0.89	C_{Mz_r}	-0.0137	0.00067	0.00083
C_{Fy_1}	-0.127	-0.321	-0.272	C_{Mz_β}	0.000208	0.00118	0.00106
				$C_{Mz_{\omega_z}}$	-0.128	-0.0192	-0.0191

The 2^{nd} and 6^{th} column shows their approximate (initial) values for both setups (i.e., without/with camera attitude reference). The 3^{rd}, 4^{th}, 7^{th} and 8^{th} columns detail their values after the 30-min long calibration/estimation phase[2], using GNSS only and GNSS plus camera-attitude aiding, respectively.

While highlighting the largest changes in color within Tab. 3 we further express the difference between the pairs of estimated VDM parameters in percentage $\Delta_{\%}$ as

$$\Delta_{\%} = \frac{|\mathbf{X}_{w_c} - \mathbf{X}_{w/o_c}|}{min\left(\mathbf{X}_{w_c}, \mathbf{X}_{w/o_c}\right)} \times 100 \tag{20}$$

where $\mathbf{X}_{w_c}$ and $\mathbf{X}_{w/o_c}$ are the states estimated with and without the addition of camera attitude reference, respectively. These relative discrepancies are depicted in Fig 6. While some coefficients change little after convergence for both methods, others change remarkably.

In particular, C_{FT_2}, C_{Fz_1} and C_{Fx_α} converge to considerably different values (magnitude-wise) when the attitude references are used (represented in red in Tab. 3). Furthermore, the sign of estimated C_{Fx_α} is reversed with respect to its initial value. Some other parameters also change their sign. These are printed in green within Tab. 3. Note that for some parameters a sign change occurred after convergence irrespective of the use of attitude updates which highlights the coarse approximation of their initial values.

Auxiliary states

As presented in Sec. 2., the other auxiliary states ($\mathbf{X}_e$ and $\mathbf{X}_w$) model the random errors for both the triplet of accelerometer and gyroscope measurements as well as the wind. We follow the setup introduced by [13] where all parameters are modeled as random walk and their initial values are set to zero with the following amplitudes: $0.02\,m/s^2$ for the accelerometers, $0.002\,rad/s$ for the gyroscopes, $2\,m/s$ for wind in the horizontal direction and $0.5\,m/s$ in the vertical direction. The estimated biases of inertial sensors at the end of the calibration phase are shown in Tab. 4 for both sets of external observations (GNSS only and GNSS + attitude observations) while Tab. 5 shows the concurrent estimation of the wind, again for both sources of aiding.

[2] just before the simulated GNSS outage starts

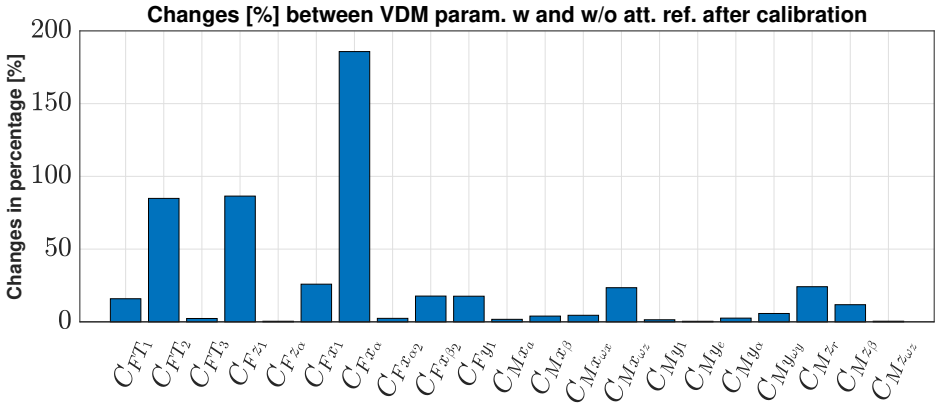

Figure 6: Percentage of change for each VDM parameter with and without the use of attitude reference measurements

These two tables indicate the correlation among the inertial systematic errors and wind estimation when only GNSS observations are used as updates during the calibration phase. The estimated value of e_{ba_1} of $-1.43\,m/s^2$ (in the flight-direction) is certainly unrealistic, nevertheless its influence gets partly absorbed by the wind estimate and partly by the C_{FT_2} and/or C_{F_α} coefficients. Similarly, the very unlikely vertical wind of $1.7\,m/s \approx 6\,km/h$ is compensated by $e_{ba_3} = 0.66\,m/s^2$ error. When attitude updates are used, the magnitude of the estimated sensor errors correspond better to the small MEMS-IMU [17] noise characteristics used during the flight without pre-calibration. At the same time, the vertical component of the wind is $\approx 1\,km/h$. A thermal airflow of this magnitude is possible in the agricultural fields and sunny conditions that were present at the experiment location.

Table 4: Estimated accelerometer and gyroscope errors for each axis at the end of the calibration phase.

States	Init. Value	Calibrated aid: GNSS only	Calibrated aid: GNSS+CAM	Changes [scale]	units
e_{ba_1}	0	-1.43	-0.015	89	
e_{ba_2}	0	0.22	-0.235	2	$[m/s^2]$
e_{ba_3}	0	0.66	0.064	9.3	
e_{bg_1}	0	-649.2	-97.1	5.7	
e_{bg_2}	0	-545.9	-35.8	14.2	$[deg/h]$
e_{bg_3}	0	214.8	-94.0	3.3	

During a standard photo mission such as the one used for calibration purposes as described in Sec. 2., the velocity of the UAV remains rather constant which complicates the separation of states influencing the forward-axis direction. Hence ideally, the calibration-phase is flown at zero-wind conditions (which was not our case) and with an IMU that has smaller systematic errors. As a solution, the uncertainty of the random switch-on IMU used in the experiment can be mitigated prior to take-off as described in [18] and thus limited to in-run instabilities, the magnitude of which are $\approx 10^{-5}\,m/s^2$ and $\approx 0.0001\,rad/s$ for the accelerometers and gyroscopes of this IMU, respectively.

Table 5: Estimated wind at the end of calibration phase.

States	Init. Value	Calibrated aid: GNSS only	Calibrated aid: GNSS+CAM	Changes [percent]	units
w_N	0	-2.96	-3.17	7	[m/s]
w_E	0	-0.336	-0.548	62	[m/s]
w_D	0	1.72	-0.31	656	[m/s]

2. Autonomous navigation

The true values of the VDM parameters remain unknown. Also as it was pointed out in the previous section, some of the estimated aerodynamic parameters may be partly absorbed by the random, yet time-correlated inertial errors. The question therefore remains, how suitable are the estimated VDM parameters for autonomous navigation. This was indirectly evaluated by simulating GNSS update outages during autonomous navigation flights. Two-min long GNSS outages were evoked at the

end of the calibration phase (IGN8) flight as well as in the two application flights (IGN6 and IGN7). The first row of Fig. 7 depicts these flights in a 2D view of the local-mapping frame. The red portion of each trajectory highlights the two-min-long GNSS-outage simulation.

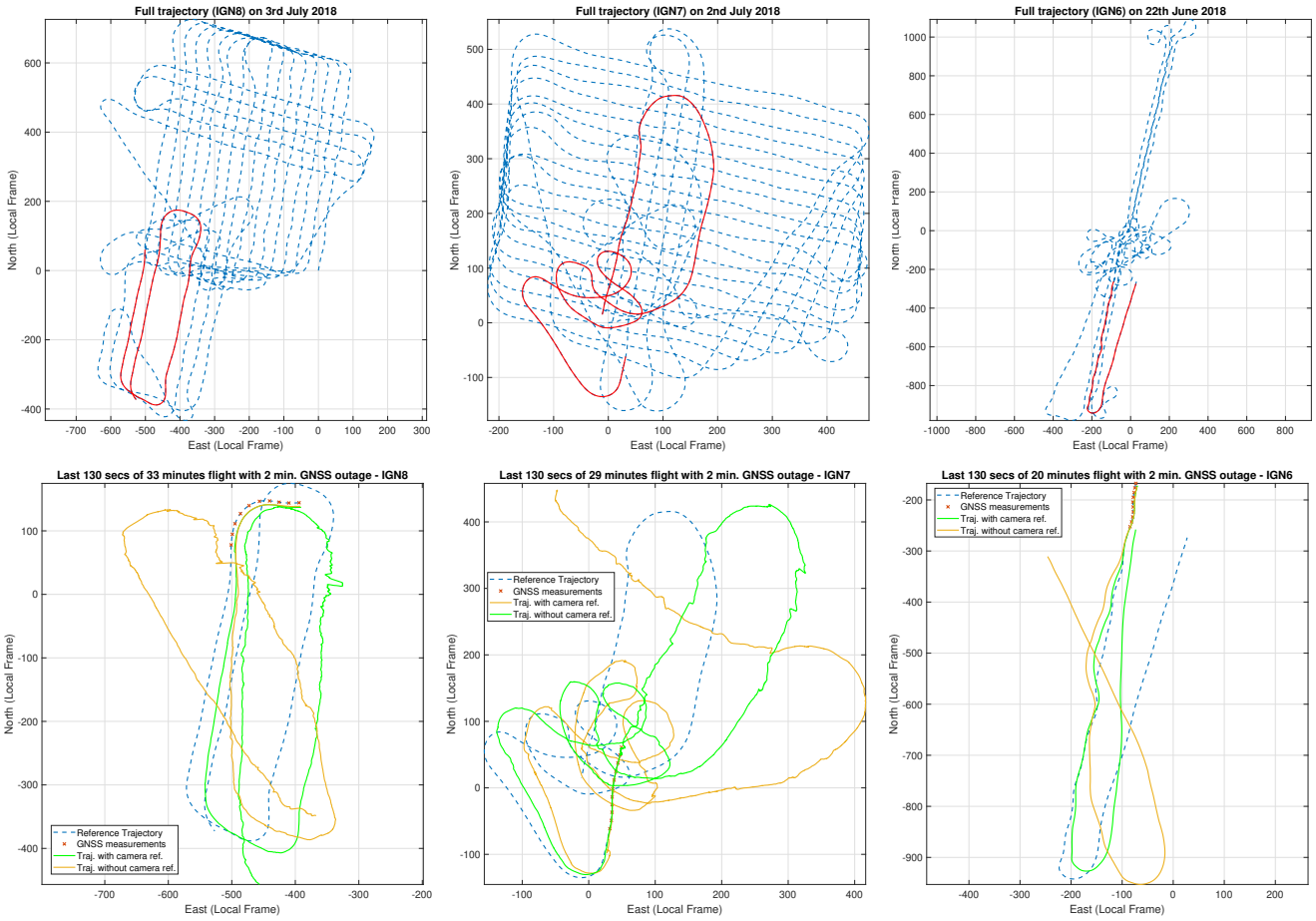

Figure 7: The three reference trajectories with the last 2 minutes of GNSS outage in red (first row). Comparison during 2-min GNSS outage of VDM-based navigation performance (middle row) using the IGN8 trained aerodynamic coefficients (green) or without (yellow).

The experimental setup used in the application flights included exactly the same aircraft and payload as used in the calibration phase. The application flights contain the following differences: a) although some photos are taken, they are no longer used, b) the flights are carried out in the same area but different flight-plans are used, so the flights lines differ in length ((IGN7) shorter, (IGN6) longer), c) the cm-level relative positioning (PPK) is used only as a reference, hence only stand-alone GNSS position and velocities are used for inertial-based (used for initialisation and in comparison) and VDM-based navigation before declaring their absence. Further, the VDM parameters $\mathbf{X}_p$ at the end of the calibration phase in the IGN8 flight for both cases (without/with att. ref.) are saved along with their corresponding correlation matrices (P). They are then used as initial states $\mathbf{X}0_p$ and covariance matrices $\mathbf{P}0_p$ for the two other application flights, IGN6 and IGN7 respectively. The initial uncertainty is increased by 1% for all aerodynamic coefficients, while the systematic IMU errors and wind are reset to zero. By doing so, new calibration phases (however, this time without attitude updates) are able to adapt the whole parameter set to a new set of sensor errors (inertial) and weather conditions.

The period of GNSS outage is highlighted in the second row of Fig. 7 where three different trajectories are shown: (i) the reference position is drawn as a dashed blue line. The portion of the trajectories when GNSS position and velocity are still available to the estimator ($\approx$ 10 seconds) are represented with red crosses; (ii) the VDM-based autonomous navigation using the aerodynamic coefficient priors from IGN8 derived without (brown) and (iii) with (green) attitude updates. It is clearly evident in the figures that the complementary information of attitude updates employed in the calibration phase of IGN8 certainly influenced positively the initial conditions of the application flights (IGN6 and IGN7) in terms of mitigating the magnitude and direction of the position drift.

Tab. 6 summarizes the navigation performance during the simulated GNSS outage for the calibration and the two validation flights (IGN8, IGN7 and IGN6). The four elements presented are (1) the error in horizontal position at the end of the two minutes of GNSS outage, (2) the root mean square error for both 2D and (3) 3D position during the whole period and, (4) the percentage of time the UAV stays within 150 m of the true trajectory. The latter criterion is useful for the UAV to return close to a safe (home) location where (i) the UAV can land or (ii) the operator can assume manual control. For the set of VDM-coefficients calibrated with the help of attitude aiding this was achieved in all tested cases.

Table 6: Position error at the end of the two-min simulated GNSS outage, 2D and 3D position RMSE and time spent within 150m of the reference trajectory during the outage.

	IGN8		IGN7		IGN6	
	w/o camera	w. cam	w/o camera	w. cam	w/o camera	w. cam
Error end traj. $[m]$	167	108	421	60.7	275	102
RMSE 2D $[m]$	97.3	46.9	133.5	62.5	68.9	30.0
RMSE 3D $[m]$	98.6	47.2	138.14	67.0	79.78	53.3
Time withing 150 m $[\%]$	77.7	100	68.1	98.8	88.7	100

For comparison, a traditional inertial-only-based navigation (INS/GNSS) with 16 states including position (3), velocity (3), attitude (4) and IMU biases for accelerometers and gyroscopes with the same initial uncertainties as for the VDM-based navigation cases (6) is performed under the same conditions with a simulated two-min GNSS outage at the end of the trajectory for the three flights. The superior performance of VDM-based navigation with respect to inertial-only navigation in the GNSS-denied environment can be observed when comparing Fig. 8 and Fig. 7.

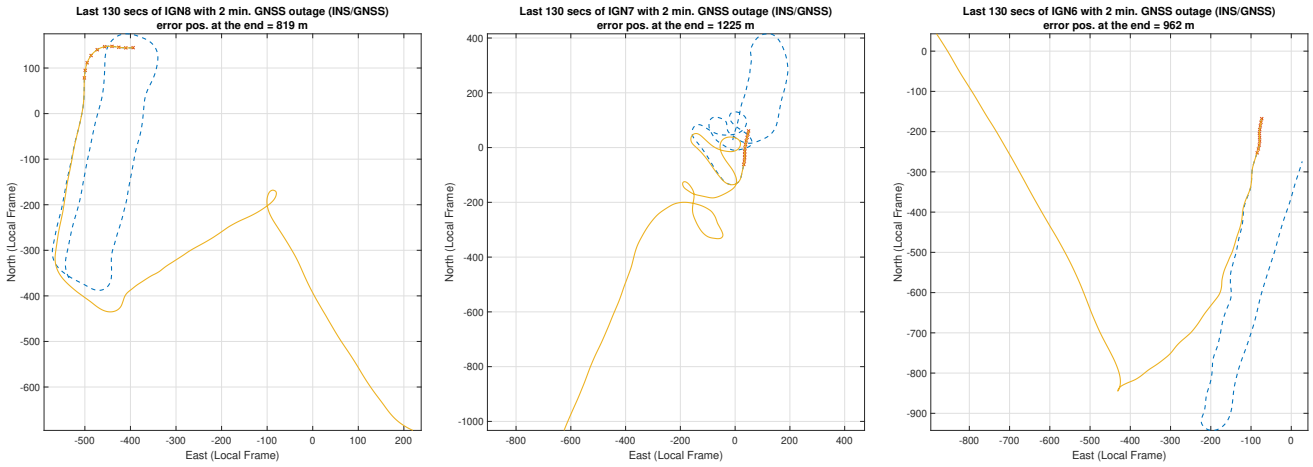

Figure 8: INS/GNSS based navigation performance under 2-min GNSS outage for the three trajectories.

VI. CONCLUSION

In this work the use of attitude references derived using photogrammetric methods in the calibration of VDM parameters has been explored. Such measurements have been gathered in a fixed calibration trajectory where more than 400 images were processed to obtain the attitude references. The inclusion of attitude references during the calibration phase revealed to improve the estimation of the aerodynamic coefficients, IMU errors and wind estimation leading to an improvement in autonomous VDM-based navigation under GNSS outage. Moreover, these results were confirmed in two additional trajectories executed with the same platform. It confirms that in general, applying such methods can improve the performance of autonomous navigation as compared to traditional INS/GNSS navigation approaches.

ACKNOWLEDGEMENTS

This research was supported by Swiss DDPS under contract 8003518612, support of which is greatly appreciated. A sincere thank you to J. R. Murray-Lahaye for his valuable English proofreading.

REFERENCES

[1] M. Khaghani and J. Skaloud, "Autonomous Navigation of Small UAVs based on Vehicle Dynamic Model," in *ISPRS - International Archives of the Photogrammetry, Remote Sensing and Spatial Information Sciences*, vol. XL-3/W4, Lausanne, Switzerland, 2016, pp. 117–122. [Online]. Available: http://www.int-arch-photogramm-remote-sens-spatial-inf-sci.net/XL-3-W4/117/2016/

[2] ——, "Application of vehicle dynamic modeling in uavs for precise determination of exterior orientation," *The International Archives of Photogrammetry, Remote Sensing and Spatial Information Sciences*, vol. 41, p. 827, 2016.

[3] ——, "Assessment of VDM-based Autonomous Navigation of a UAV under Operational Conditions," *Robotics and Autonomous Systems*, vol. 106, pp. 152 – 164, 2018.

[4] ——, "Vdm-based uav attitude determination in absence of imu data," in *European Navigation Conference (ENC 2018)*. IEEE, August 2018, pp. 84–90.

[5] M. Rehak and J. Skaloud, "Fixed-wing Micro Aerial Vehicle for Accurate Corridor Mapping," in *ISPRS Annals of Photogrammetry, Remote Sensing and Spatial Information Sciences*, vol. II-1/W1, Toronto, Canada, 2015, pp. 23–31. [Online]. Available: http://www.isprs-ann-photogramm-remote-sens-spatial-inf-sci.net/II-1-W1/23/2015/

[6] J. Skaloud and K. Legat, "Theory and reality of direct georeferencing in national coordinates," *ISPRS Journal of Photogrammetry and Remote Sensing*, vol. 63, no. 2, pp. 272–282, 2008.

[7] D. Cucci and S. J., "Joint adjustment of raw inertial data and image observations: methods and benefits," in *Photogrammetric Week*, 2019, p. 8.

[8] A. Gelb, Ed., *Applied Optimal Estimation*. Cambridge, Massachusetts, USA: The MIT Press, 1988.

[9] M. Khaghani and J. Skaloud, "Autonomous Vehicle Dynamic Model-Based Navigation for Small UAVs," *Navigation*, vol. 63, no. 3, pp. 345–358, 2016.

[10] N. Rösch, "Rotations, quaternions and double groups. by simon l. altmann, clarendon press, oxford, 1986, 317 pp." *International Journal of Quantum Chemistry*, vol. 32, no. 3, pp. 401–401, 1987.

[11] J. B. Kuipers *et al.*, *Quaternions and rotation sequences*. Princeton university press Princeton, 1999, vol. 66.

[12] G. J. Ducard, *Fault-tolerant flight control and guidance systems: Practical methods for small unmanned aerial vehicles*. London: Springer, 2009.

[13] M. Khaghani and J. Skaloud, "Evaluation of Wind Effects on UAV Autonomous Navigation Based on Vehicle Dynamic Model," in *Proceedings of the 29th International Technical Meeting of The Satellite Division of the Institute of Navigation (ION GNSS+ 2016)*, Portland, Oregon, USA, 2016, pp. 1432–1440.

[14] O. Martin, C. Meynard, M. Pierrot Deseilligny, J.-P. Souchon, and C. Thom, "Réalisation d'une caméra photogrammétrique ultralégère et de haute résolution," in *Proceedings of the colloque drones et moyens légers aéroportés d'observation, Montpellier, France*, 2014, pp. 24–26.

[15] T. Kluter, *GECKO4NAV Technical Reference Manual*, 1st ed., HuCE-mircroLab, Bern University of Applied Sciences, 2013.

[16] E. Cledat, D. A. Cucci, and J. Skaloud, "Camera calibration models and methods in corridor mapping with uavs," *ISPRS Annals of the Photogrammetry, Remote Sensing and Spatial Information Sciences*, vol. V-1-2020, pp. 231–238, 2020.

[17] Intersense, "Navchip," http://www.intersense.com/pages/16/246, accessed 2015-12-10.

[18] P. Clausen and J. Skaloud, "On the calibration aspects of mems-imus used in micro uavs for sensor orientation," in *IEEE-ION Position Location and Navigation Symposium (PLANS)*. 1457-1466, 2020. [Online]. Available: https://doi.org/10.1109/PLANS46316.2020.9110160